Fractal and lacunarity analyses: quantitative characterization of hierarchical surface topographies

Edwin Jee Yang **Ling**

Phillip **Servio**

Anne-Marie **Kietzig***

Department of Chemical Engineering, McGill University, 3610 University Street, Montréal, Québec, H3A 0C5, Canada

*Corresponding author. Tel: +1(514) 398-3302. E-mail: anne.kietzig@mcgill.ca

Authors' last names are indicated in **bold**.

Abstract

Biomimetic hierarchical surface structures that exhibit features having multiple length scales have been used in many technological and engineering applications. Their surface topographies are most commonly analyzed using scanning electron microscopy (SEM), which only allows for qualitative visual assessments. Here we introduce fractal and lacunarity analyses as a method of characterizing the SEM images of hierarchical surface structures in a quantitative manner. Taking femtosecond laser-irradiated metals as an example, our results illustrate that, while the fractal dimension is a poor descriptor of surface complexity, lacunarity analysis can successfully quantify the spatial texture of an SEM image; this, in turn, provides a convenient means of reporting changes in surface topography with respect to changes in processing parameters. Furthermore, lacunarity plots are shown to be sensitive to the different length scales present within a hierarchical structure due to the reversal of lacunarity trends at specific magnifications where new features become resolvable. Finally, we have established a consistent method of detecting pattern sizes in an image from the oscillation of lacunarity plots. Therefore, we promote the adoption of lacunarity analysis as a powerful tool for the quantitative characterization of, but not limited to, multi-scale hierarchical surface topographies.

Keywords: Fractal dimension; lacunarity; hierarchical surfaces; texture analysis; laser-induced surface topographies; scanning electron microscopy

1. Introduction

Biomimetic-inspired hierarchical surfaces have received significant attention as a means of altering the surface properties of metals, semiconductors, and polymers (Bhushan, et al., 2009; Ellinas, et al., 2011; Kietzig, et al., 2009; Noh, et al., 2010; Nosonovsky & Bhushan, 2008). Historically, many attempts have been centered upon replicating the lotus leaf (*Nelumbo nucifera*), whose dual-scale surface topography consisting of micrometer-sized papillose epidermal cells covered by sub-micron epicuticular waxes, render it superhydrophobic (Barthlott & Neinhuis, 1997). Today, various synthetic hierarchical surfaces have been successfully fabricated on metallic, polymer, and semiconductor specimens using a range of techniques (Bhushan, 2012; Feng, et al., 2011; Kietzig, et al., 2009; Nakayama, et al., 2014) for applications in self-cleaning materials (Wang, et al., 2013), improved light harvesting in dye-sensitive solar cells (Shao, et al., 2011), drag reduction (Jung & Bhushan, 2010), catalysis (Neumann & Hicks, 2012; Zhang, et al., 2011), and enhanced adhesion (Ho, et al., 2011), to name a few.

The most frequently used technique for characterizing and reporting surface topography is scanning electron microscopy (SEM), which provides a visual representation of the micro- and nano-scale surface features. The major drawback associated with SEM, however, is that it only provides a qualitative assessment of the surface texture. Attempting to compare or rank SEM images of surface topographies on the basis of visual inspection alone is deficient since it is often performed subjectively and intuitively. Nevertheless, this is common practice in the field of surface topography modification due to its convenience (Ahmmed, et al., 2015; Moradi, et al., 2013; Nayak & Gupta, 2010; Zhang, et al., 2006). For example, Zhu *et al*. (Zhu, et al., 2011) compared the changes in the flower-like morphology of anatase TiO_2 with respect to different hydrothermal reaction and calcination times by only utilizing SEM images. To mitigate the qualitative nature of visual topography analysis, some authors supplement SEM imaging by measuring the surface roughness (e.g. R_a) via profilometry, atomic force microscopy (AFM), or confocal microscopy (Demir, et al., 2014; Jagdheesh, et al., 2011; Zou, et al., 2011). This is an imperfect solution, however, given that roughness measurements cannot fully describe the morphology of the surface structures, nor can they identify the presence of hierarchical structures.

In this work, we introduce fractal and lacunarity analyses as a method of quantifying the complexity and texture of surface topographies containing hierarchical structures. The hierarchical surface structures analyzed in this study are fabricated by femtosecond (fs) laser processing of metallic samples, which yields both randomly organized (laser-induced) and regular (laser-inscribed) surface features containing multiple length scales (Ahmmed, et al., 2014; Ling, et al., 2015). Once the SEM images of laser-induced and laser-inscribed topographies have been quantified via fractal and lacunarity analyses, they can be characterized and compared in an objective manner. This, in turn, provides a convenient means of reporting changes in surface topography with respect to changes in processing parameters. In addition, our examination of fractal image processing techniques provides insight into how to better interpret fractal-based descriptors of texture, specifically lacunarity, and its dependence on scale and pattern sizes.

2. Background

When a specimen is analyzed using SEM, secondary electrons emitted from its surface are collected to generate an image that captures the appearance of its surface topography. These images, which are essentially a collection of pixels of various intensities grouped in a particular order, provide information regarding the surface texture (an appearance), rather than its roughness (a property) (Davies, 2008). Strictly speaking, an image is referred to as a texture when it contains an uncountable number of texture elements that exhibit both a random and regular arrangement (Davies, 2008). Therefore, texture, or spatial analysis, is often carried out using statistical measures (Dale, 2000; Dale, et al., 2002; Davies, 2008) since it involves identifying patterns within large data sets. Numerous spatial analysis techniques exist, such as the co-occurrence matrix, Fourier transform, wavelet transform, variance-to-mean ratio method, and three-term local quadrat variance (3TLQV) (Bharati, et al., 2004; Dale, et al., 2002; Davies, 2008; Tuceryan & Jain, 1998). In this study, we will utilize fractal mathematics to quantify the complexity and spatial heterogeneity of an image.

2.1. Fractals

The complex shapes and textures found in nature cannot be easily described using ideal primitive shapes (circles, squares, spheres, etc.) (Sarkar & Chaudhuri, 1994). Fractal geometry was developed by Mandelbrot (Mandelbrot, 1983) as a means of tackling these irregular non-Euclidean and non-differentiable objects, such as Cantor dusts, space-filling Peano curves, the Koch snowflake (shown in Figure 1a), and Brownian motion. Fractals are mathematical sets or objects that exhibit self-similarity at every magnification or scale; this is also known as scale invariance (Falconer, 1990; Jelinek & Fernandez, 1998; Mandelbrot, 1983; Pentland, 1984). Natural sceneries and surfaces (clouds, mountains, coastlines, and lightning, for example) have been observed to exhibit fractal features and can be approximated by fractal functions over a limited range of scales (typically three to four orders of magnitude) (Cutting & Garvin, 1987; Mandelbrot, 1983; Pentland, 1984). Similarly, hierarchical surface features produced by advanced processing techniques (chemical etching, self-assembly, lithography, etc.) can be characterized by fractal analysis by using two statistical measures known as the fractal dimension (D_F) and lacunarity (λ). Image analysis that employs the use of fractals has been used in many areas (Al-Kadi & Watson, 2008; Jelinek & Fernandez, 1998; Karperien, et al., 2013; Updike & Nowzari, 2008; Uppal, et al., 2010; Yaşar & Akgünlü, 2005), including image segmentation (Dubuisson & Dubes, 1994; Keller, et al., 1989) and the classification of ecological (Kenkel & Walker, 1993; Malhi & Román-Cuesta, 2008) and urban (Myint & Lam, 2005) spatial distributions.

2.2. Fractal dimension

In conventional Euclidean space, objects may only exist in integer dimensions, i.e. 0-dimension refers to a point, 1-dimension to a line, 2-dimensions to a surface, and 3-dimensions to a volume. Classical mensuration equations for calculating the area or volume of an object can be generalized to

$$M = An^D \tag{1}$$

where M is the desired metric property (area or volume), A is a constant, n is the size of the measuring instrument, and D is the relevant Euclidean dimension (Pentland, 1984). In the case of a fractal curve such as the Koch snowflake in Figure 1a, however, its true perimeter is infinite because the perceivable detail of its boundary increases forever with increasing scale. Instead of characterizing these fractal objects with classical measures of perimeter and area, mathematicians introduced fractional, or fractal dimensions (D_F), which can take non-integer values (Mandelbrot, 1983):

$$D_F = \frac{\ln N(r)}{\ln(r)} \tag{2}$$

$N(r)$ refers to the number of new details and r represents the scaling used to arrive at those new details. According to Equation (2), D_F is the ratio of an object's level of detail to changes in scaling; in other words, it signifies how much new detail can be perceived as the object is viewed at higher and higher magnifications. It can thus be viewed as a measure of roughness or complexity, where a larger D_F indicates greater complexity. The non-integer dimensional values essentially compensate for the details that are lost in Equation (1) since they are smaller than the size of the measuring instrument, *n*. In the case of the Koch curve in Figure 1a, for example, the theoretical D_F = log 4/log 3 = 1.2619. Since D_F falls in between the Euclidean, or topological, dimensions 1 and 2, the Koch curve can be described as being "between" a straight line ($D = 1$) and a plane ($D = 2$).

There are several ways to estimate D_F from an image, including the mass-radius, dilation, cumulative intersection, and box-counting methods (Jelinek & Fernandez, 1998), the latter of which is the most frequently used. The description of the box-counting method that follows assumes that the image under analysis is a binary image that only contains 1's (white pixels) and 0's (black pixels), which are the foreground and background, respectively. Non-overlapping boxes of size r x r are overlain on the image, and the number of boxes that contain foreground pixels $N(r)$ are counted. The box sizes are reduced, which results in a functional relationship between $N(r)$ and r. The slope of the log-log plot of $N(r)$ against r yields the value of D_{BC}, which is an estimate of D_F using the box-counting method (Chen, et al., 1993; Keller, et al., 1989). By calculating D_{BC} for different images, it is possible to compare their inherent roughness and complexities in a quantitative manner. One major drawback with regards to using D_F is that it is not a unique and sufficient measure, i.e. two images that appear largely different may yield the same D_F due to similarities in roughness (Dubuisson & Dubes, 1994; Gårding, 1988; Plotnick, et al., 1993; Smith Jr, et al., 1996). Additional quantitative properties of images are thus needed in order to better facilitate their characterization. One such measure is lacunarity, which computes the spatial heterogeneity of an image (Mandelbrot, 1983).

2.3. Lacunarity (λ)

Mandelbrot aptly declared texture as an abstract and elusive notion that cannot be easily grasped, let alone quantified (Mandelbrot, 1983). He introduced lacunarity (*lacuna*, which in Latin means "gap") as a means of measuring texture, or more specifically, spatial heterogeneity (Mandelbrot, 1983). A more rigorous definition of lacunarity is given by Gefen *et al*. (Gefen, et al., 1983), who states that it is the measure of the deviation of an object or fractal from translational invariance (Plotnick, et al., 1993). Objects with higher lacunarity are more spatially coarse or "clumped", while lower lacunarity values correspond to an area exhibiting a finer texture. The most common algorithm used to calculate the lacunarity of images is the gliding box-counting (GBC) method developed by Allain and Cloitre (Allain & Cloitre, 1991).

A box of size r x r is placed on the top left corner of a binary image of size M x M, as shown in Figure 1b. The number of foreground pixels in the box of size r is counted. The box is then moved to the right by a distance Δr (typically one or two pixels), and the number of foreground pixels are counted again. This procedure is repeated until the entire image has been covered by the gliding box, where the total number of boxes used is designated as $N(r)$. Then, the probability distribution of obtaining k foreground pixels in a box of size r is given by:

$$Q(k, r) = \frac{n(k, r)}{N(r)} \tag{3}$$

where $n(k, r)$ is the number of boxes of size r that contain k foreground pixels. The first and second moments of the mass probability distribution are then calculated by

$$Z_1(r) = \sum_{k=0} k\,Q(k, r) \tag{4}$$

$$Z_2(r) = \sum_{k=0} k^2\,Q(k, r) \tag{5}$$

The lacunarity, $\lambda(r)$, is then determined as follows:

$$\lambda(r) = \frac{Z_2(r)}{[Z_1(r)]^2} \tag{6}$$

which can also be rewritten as

$$\lambda(r) = \left[\frac{s_k(r)}{\bar{k}(r)}\right]^2 + 1 \tag{7}$$

where $\bar{k}(r)$ and $s_k(r)$ are the mean and standard deviation of the number of foreground pixels for box size r. Inspection of Equation (7) shows that $\lambda(r)$ measures the ratio of the standard deviation of the probability distribution of foreground pixels to its mean for a particular r, which indicates that $\lambda(r)$ increases as the image becomes more spatially heterogeneous (greater variance).

Equations (3)-(7) illustrate two more properties of $\lambda(r)$. Firstly, $\lambda(r)$ is a function of the box size r, and it is therefore recommended to display $\lambda(r)$ as a function of a wide range of box sizes instead of merely comparing values of $\lambda(r)$ at an arbitrary box size (Plotnick, et al., 1996; Plotnick, et al., 1993). Secondly, the highest value $\lambda(r)$ is obtained when $r = 1$ since $Q(k=1,r=1) = P$, where P is the total number of foreground pixels divided by the total number of pixels. Then from Equations (4)-(6), one arrives at $\lambda(r=1) = 1/P$. Thus, $\lambda(r=1)$ only depends on the proportion of foreground pixels relative to the entire image (Plotnick, et al., 1996; Plotnick, et al., 1993). On the other hand, when r approaches the image size M, the normalized standard deviation of the number of foreground pixels approaches zero, and thus $\lambda(M)$ tends to unity, from Equation (7) (Plotnick, et al., 1996).

There are several studies that have already used fractal and lacunarity analyses to extract information from electron microscopy images (Alvarez, et al., 2013; Khorasani, et al., 2011; Manera, et al., 2014). For example, Utrilla-Coello *et al*. (Utrilla-Coello, et al., 2013) investigated the micro-scale morphology of retrograded starch, and, using D_F and λ, were able to quantify observed changes in their SEM images with respect to storage time and temperature. Also, Rivera-Virtudazo *et al*. (Rivera-Virtudazo, et al., 2009) measured the degree of clumping of heat-treated hybrid organosilica materials from transmission electron microscope (TEM) images using lacunarity plots. In Section 4.1, we apply both fractal and lacunarity analyses to quantify and compare SEM images of surface topographies produced by fs-laser irradiation. We show that while the D_F is a poor descriptor of surface complexity, lacunarity is a viable technique for the analysis of SEM images in the field of laser surface texturing.

In Section 4.2, we investigate the utility of $\lambda(r)$ in characterizing hierarchical structures. The analysis of hierarchical sets has already been performed using lacunarity, spectral (Fourier) and wavelet transforms (Saunders, et al., 2005; Workman, et al., 2015). The latter approach has been shown to be superior to both lacunarity and Fourier transforms (Saunders, et al., 2005), because discrete wavelet transforms (DWT) decompose an image into multiple detail levels, making it a suitable technique for analyzing multi-scale hierarchical structures (Palazoglu, et al., 2010; Workman, et al., 2015). However, we show in Section 4.2 that by analyzing multiple SEM images of a hierarchical surface at different magnifications, lacunarity plots are in fact sensitive to multiple length scales present in hierarchical structures. Finally, in Section 4.3, we provide new information on how lacunarity plots can be used to detect pattern sizes present within images by examining the period at which $\lambda(r)$ oscillates.

3. Methods

Metallic specimens were irradiated by an 800 nm amplified Ti:Sapphire laser (Coherent Libra). The Gaussian beam had a pulse duration of <100 fs and a repetition rate of 10 kHz. Laser-induced surface topographies were fabricated on stainless steel 304 (McMaster-Carr) and aluminum (Alloy 2024, McMaster-Carr) by mounting the samples onto a linear translation stage (Zaber Technologies, Inc.) that manipulated the samples in a raster scan pattern beneath the incident beam at a velocity v. The output power of 4 W was reduced to the desired processing power P by a variable attenuator comprised of a half wave-plate and a polarizing beam splitter. The sample machining plane relative to the focal point (Δy) was varied in order to obtain different types of laser-induced features. In this study, the machined surface was maintained between the focal point and the focusing lens, or $\Delta y \geq 0$. The $1/e^2$ theoretical beam diameter at the focal point was 31 μm. Some of the samples were scanned more than once, and the number of laser passes over the sample is denoted by N_s.

Laser-inscribed square pillars were fabricated on copper specimens (99.90% purity, McMaster-Carr) mounted on a high-precision three-dimensional linear translation stage controlled by an XPS motion/driver controller (Newport Corp.). The trajectories of the stage movements were programmed and executed by the Gol3D software (GBC&S). The Gol3D software also synchronized the XPS controller with a Uniblitz® shutter system (Vincent Associates®) composed of a 25 mm aperture shutter and a shutter driver. The laser power was attenuated to 800 mW (pulse energy of 80 μJ) and the translation velocity of the stages was maintained at 2 mm/s. The sample surface was placed at Δy = -0.73 mm and scanned five times (N_s = 5).

After laser processing, the samples were cleaned with acetone in an ultrasonic bath for five minutes. The surface topographies of the laser-irradiated areas were imaged in an SEM (Phenom-World and FEI Inspect F50) using an accelerating voltage of 5.0 kV and a probe current of approximately 0.1 nA. Although one image was acquired per sample, we know, based on previous work, that the surface topographies imparted by fs-laser surface texturing under the specified experimental conditions were homogeneous, i.e. the morphology of the surface features was uniform in all laser-irradiated areas (Ahmmed, et al., 2015; Ling, et al., 2015). Therefore, the SEM images shown in this work, which only capture a portion of the laser-treated area, are representative of the surface topography found in the entire irradiated patch. However, the SEM images obtained at high magnification in Section 4.2 display highly random nano-scale structures that differ from one point to another within the laser-irradiated areas; we will address this issue in Section 4.2. During image acquisition, the brightness and contrast of the SEM images were painstakingly adjusted so as to minimize the differences in appearance among them, and to ensure consistency during grayscale-to-binary conversion.

The fractal analysis of SEM images, as explained in Section 2, was performed using *FracLac*, a software plugin developed by Karperien (Karperien, 1999-2014) for *ImageJ* (Rasband, 1997-2014). In order to perform fractal analysis on SEM images, they were converted from grayscale to binary format. The grayscale SEM images were transformed by first equalizing their histograms, followed by a conversion to binary format using a threshold of 0.5. This method was chosen so as to ensure that the number of foreground (white) pixels was approximately equal to the number of background (black) pixels for all images (P = 0.5).

4. Results and Discussion

4.1. Fractal analysis of surface topographies

Figures 2a to 2e display five different surface topographies that were obtained on metallic substrates, along with their fractal dimensions and lacunarity plots. Details on the fabrication of dual-scale surface topographies on metallic substrates can be found in our previous work (Ahmmed, et al., 2015). The values of D_{BC} of the five images are very similar to each other; in fact, all the calculated values of D_{BC} in this work lie within the range of 1.85-1.92, from which no discernible trend can be detected. This is because, for binary images, the fractal dimension is more suited to quantifying the complexity of single objects (Cutting & Garvin, 1987; Jelinek &

Fernandez, 1998), whereas the SEM images in Figure 2 contain multiple objects that constitute a spatial pattern, or texture. Hence, analyzing textured surfaces is better accomplished by lacunarity analysis (Figure 2) since it involves a collection of texture elements arranged in a particular order.

The log-log graphs of $\lambda(r)$ versus r in Figure 2 successfully capture the increasing spatial heterogeneity of Figures 2a to 2e. Since the undulating grooves on stainless steel 304 (Figure 2a) exhibit the finest texture in comparison to the other four topographies, its lacunarity is the lowest of the five plots. The columnar structures in Figure 2b are larger and more well-defined than the undulating grooves in Figure 2a. As a result, the foreground pixels representing the columnar structures in Figure 2b are clumped together, whereas the foreground and background pixels of Figure 2a are relatively evenly distributed throughout the image. The grouping of foreground pixels in Figure 2b thus leads to a higher pixel variance-to-mean ratio, which in turn results in a higher lacunarity, $\lambda(r)$, than that of Figure 2a. The average feature size of the columnar structures in Figure 2b is smaller than that of the maze-like structure in Figure 2c, which in turn is smaller than the layered bumps in Figure 2d. Finally, the surface topography displayed in Figure 2e exhibits large holes that result in the greatest extent of spatial clumping among the five images.

Lacunarity analysis can also be used to track the evolution of a specific type of surface topography within a range of experimental parameters. Ahmmed *et al*. (Ahmmed, et al., 2015) showed that when columnar structures are re-scanned by fs-laser pulses several times, they become more uniform, aligned and well-defined. Figure 3 illustrates the effect of multiple laser scans on the laser-induced surface topography of stainless steel 304. At N_s = 1 (Figure 3a), only undulating grooves are observed. Columnar structures are then obtained for N_s = 5 in Figure 3b, which increase in size and uniformity with greater N_s. Evidently, the most significant change in surface topography occurs between N_s = 1 and N_s = 5, and this is captured by the $\lambda(r)$ plots in Figure 3. The $\lambda(r)$ curve for Figure 3a has a much lower lacunarity than the $\lambda(r)$ curve of Figure 3b.

Although the $\lambda(r)$ plots for N_s = 5, 10, and 50 are in very close proximity to each other, close inspection reveals that the $\lambda(r)$ curves increase slightly with increasing N_s. This indicates that the surface topography of laser-irradiated stainless steel 304 becomes more spatially heterogeneous (less translationally invariant) when more laser passes are applied. Since the columnar structures are larger and more well-defined at higher N_s, the foreground pixels that represent them are clustered together in larger-sized clumps, and this in turn increases the size of the gaps (background pixels) between groups of foreground pixels. This increases the coarseness of the image, which results in a higher lacunarity.

Displaying $\lambda(r)$ as a function of r is preferred over reporting one value of λ at some arbitrary r because the shape of the $\lambda(r)$ curve provides information regarding the spatial distribution within an image (Plotnick, et al., 1993). For example, the shape of the $\lambda(r)$ curve for Figure 3a typically occurs for images in which the foreground pixels are randomly distributed throughout the image (Butson & King, 2006; Dale, 2000; Plotnick, et al., 1996; Plotnick, et al., 1993). This is consistent with the fine texture captured by the SEM image of the undulating grooves (Figure 3a). One approach of generating a single lacunarity index from $\lambda(r)$ plots is to compute the area under the curve (Utrilla-Coello, et al., 2013). That is, if $\rho(r)$ = ln r, then the degree of spatial heterogeneity, Θ, is given by:

$$\Theta = \int_0^{\ln M} \ln \lambda(\rho(r))\, d\rho(r) \tag{8}$$

where M refers to the smaller image dimension. The integral in Equation (8) is computed for the lacunarity plots in Figure 3 by numerical integration, and the results are displayed in Table 1.

Θ provides a convenient measure of the degree of spatial heterogeneity of an image. From Table 1, Θ increases considerably from 0.72 to 1.54 between Ns = 1 and 5 due to the abrupt change in surface topography (Figures 3a and 3b). On the other hand, the slight change in surface topography for N_s = 5, 10, and 50 is reflected in the small increase in Θ. Figure 3 and Table 1 show how lacunarity analysis is suitable for detecting even small changes in topography, which would otherwise be difficult to confirm based on qualitative assessments alone.

Figures 2 and 3 clearly demonstrate that quantifying the laser-induced surface topographies using lacunarity analysis provides an objective method of comparing spatial texture. However, because $\lambda(r)$ is only a measure of the degree of translational invariance within an image, the comparison of surface topographies with distinctly different appearances should be avoided. Furthermore, inferring the surface topography based on $\lambda(r)$ curves alone is discouraged since lacunarity analysis does not distinguish between the different shapes and structures present within an image.

4.2. Hierarchical structures and lacunarity

Complexity and texture are heavily scale-dependent: a particular surface topography may appear coarse at one magnification but very fine at a lower viewing magnification (Davies, 2008), i.e. texture analysis must be performed in a relative fashion. Texture analysis is further complicated by topographies exhibiting features having multiple length scales, such as metallic specimens irradiated by fs-laser pulses (Ahmmed, et al., 2014; Ahmmed, et al., 2015; Kietzig, et al., 2009; Lehr & Kietzig, 2014; Ling, et al., 2015). Most studies have attempted to extract hierarchical information from one dataset at only one scale of viewing. In this case, the features containing the larger lateral dimension dominate the output parameter, resulting in the omission of features at lower length scales (Workman, et al., 2015). In addition, if a hierarchical object contains features whose length scales differ largely (say, more than one order of magnitude), then the smaller features will not be well resolved in the image due to limitations in the sampling instrument.

The straightforward alternative is to image the surface at multiple magnifications instead of trying to extract hierarchical information solely from one image. Hence, we proceeded to investigate how lacunarity analyses are influenced by the magnification under which SEM images of laser-irradiated surface patterns are obtained. Hierarchically structured laser-inscribed square pillars (84.8 ± 1.7 μm side length) were micromachined on copper, which were imaged at different magnifications ranging from 150x to 120,000x. The lacunarity analysis of SEM images of the laser-inscribed square pillars is shown in Figure 4.

The $\lambda(r)$ plots in Figure 4 can be divided into three broad regimes. In Figure 4a, $\lambda(r)$ increases steadily for 150x to 1500x. From 1500x-15,000x, however, the lacunarity of the SEM images decreases with increasing magnification, as seen in Figure 4b. Finally, Figure 4c shows that $\lambda(r)$ increases once again for higher magnifications, between 15,000x and 120,000x. Evidently, not only does the lacunarity of the surface topography vary greatly with scale, its trend with respect to increasing magnification reverses within certain scale intervals.

The SEM image captured at 150x, shown in Figure 4a, is essentially an array of square pillars. At this magnification, each pillar is 44 ± 0.6 pixels wide, which makes up approximately 0.2% of the entire image area. At 300x, each square pillar accounts for 0.8% of the total image, but by 1500x (SEM shown in Figure 4a), only one complete square pillar remains, which occupies about a quarter of the total image. As a result, the lacunarity of the images increases with scale since the size of the pillars (in pixels), and hence the spatial heterogeneity, increases. Under low magnification, say 150x, the SEM image is only able to resolve details in the range of

50-100 μm since 1 pixel represents approximately 2 μm. At higher magnification, on the other hand, the minimum resolvable detail increases and previously indistinguishable features become perceivable. From Figure 4, this “turning point” occurs at 1500x since the lacunarity begins to decrease from here onwards.

There are two reasons that the lacunarity starts to decrease beyond 1500x in Figure 4b. Firstly, as the square pillar gradually fills the screen, the area surrounding the single pillar, which is composed of background pixels, shrinks. This reduces the spatial heterogeneity of the image. Secondly, micrometer length scale features become progressively distinguishable after 1500x. Since they are still small in relation to the entire image area, the SEM image exhibits a fine texture. However, comparison of Figures 4a and 4b indicates that the SEM image at 15,000x is more spatially heterogeneous than that taken at 150x since the latter has a lower lacunarity than the former. At 15,000x in Figure 4b, the $\lambda(r)$ plot assumes a linear slope, which suggests that the surface topography at that scale exhibits self-similarity (Allain & Cloitre, 1991). It is also at this point where the lacunarity begins to increase with scale again.

Nano-scale features (redeposited nanoparticles, in this case) that were indiscernible at 1500x become resolved at 15,000x. These nanoparticles increase in size with increasing magnification, resulting in greater spatial heterogeneity. As a result, the lacunarity increases until we reach the microscope’s magnification limit at 120,000x. At magnifications greater than 1500x, the surface features become increasingly random and will inevitably differ from other areas within the same patch. This does not, however, alter the fact that the lacunarity trends will still reverse whenever new features become resolvable. We applied the same analysis in Figure 4 to a completely different laser-inscribed square pillar topography machined under different conditions and observed the same lacunarity trend reversals; this is illustrated in Figure S1 from the accompanying Supplemental Materials. Figure 4 demonstrates that the lacunarity trends reverse with every change in the order of magnitude of the magnification due to the introduction of new detail at larger scales. At 150x, the SEM image displays objects on the order of 100 μm. Then at 1500x, features on the order of 10 μm are resolvable, followed by 1 μm features at 15,000x, and finally 100 nm features at 120,000x.

In contrast to the findings of several authors (Dale, 2000; Saunders, et al., 2005), who stated that lacunarity analyses could not consistently distinguish between sets containing multiple scales, the results in Figure 4 illustrate how lacunarity plots can be used to determine the scaling at which new features become resolvable. One additional advantage of using $\lambda(r)$ to characterize hierarchical structures is that it can characterize both regularly and randomly shaped hierarchical features. For example, the square pillars (~100 μm) are highly ordered and thus their surface profile could be measured easily, but the micro- and nano-scale structures on top of the pillars, which are gnarled and randomly distributed, are more difficult to characterize. Many hierarchical surfaces that have been reported in literature contain well-defined micro-scale features decorated by irregularly shaped nanometer-length structures (Ahmmed, et al., 2014; Ellinas, et al., 2011; Gerasopoulos, et al., 2012; Ling, et al., 2015; Noh, et al., 2010). Furthermore, lacunarity analysis can also be extended to hierarchical surface topographies that contain irregularly shaped and randomly distributed features on all scales, with the ability to distinguish between different length scales.

4.3. Lacunarity dependence on pattern sizes

Another characteristic of $\lambda(r)$ plots was raised by Plotnick *et al.* (Plotnick, et al., 1996). They stated that when the size of a certain “random pattern” corresponds to some critical box size r_c, then $\lambda(r > r_c)$ begins to decline rapidly. This property of lacunarity plots allows for the estimation of the average size of a "random pattern" within an image. Dale (Dale, 2000), however, found that pattern sizes cannot be consistently and accurately determined from plots of $\lambda(r)$ because its slope tends to change smoothly rather than abruptly. Since the laser-inscribed square pillars observed in this work are regularly spaced and have uniform widths, the $\lambda(r)$ plots should be able to detect their size easily according to the guidelines given by Plotnick *et al*. (Plotnick, et al., 1996). The square markers in Figure 4a indicate the measured pixel widths r_{pillar} of the square pillars. Here we see that $\lambda(r = r_{pillar})$ for each plot occurs near unity, but certainly not when the lacunarity plot begins to decline rapidly. In fact, it is not immediately obvious whether there is a characteristic "break-point" r_c in the $\lambda(r)$ curve that one could use to identify the size of a random pattern. Since the laser-inscribed square pillars in this work (Figure 4) have a well-defined pattern size, we investigated how $\lambda(r)$ plots change with images containing different pattern sizes.

The $\lambda(r)$ curves shown in Figure 4a oscillate near 1 for large box sizes. This is a distinctive feature of regularly spaced spatial patterns and has also been observed elsewhere (Dale, 2000; Plotnick, et al., 1996), but no comprehensive explanation for their occurrence has been given yet. These oscillations can be explained by examining the means and standard deviations of the pixel distributions, $\bar{k}(r)$ and $s_k(r)$, respectively. Figure 5a shows the values of $\bar{k}(r)$ and $s_k(r)$ as a function of r for an SEM image of the laser-inscribed square pillars taken at 300x magnification.

The mean number of pixels increases monotonically with r since the gliding box covers a larger number of pixels. However, since P = 0.5 for all images due to the grayscale-to-binary conversion scheme outlined in the Materials and Methods, the normalized mean, $\bar{k}(r)/r^2$, is equal to P. This can be verified by plotting $\bar{k}(r)$ against r^2, which yields a slope equal to P. Substituting this result into Equation (7) and rearranging, we arrive at:

$$\lambda(r) = \frac{1}{P^2}\left[\frac{s_k(r)}{r^2}\right]^2 + 1 \tag{9}$$

Equation (9) shows that the lacunarity of an image with constant P only depends on $[s_k(r)/r^2]^2$, which is the normalized pixel variance. Hence, $\lambda(r)$ is essentially a measure of degree of variation in the number of foreground pixels counted in the gliding box.

The plot of $s_k(r)$ against r reveals a large degree of oscillation with an approximate period of r = 110 pixels. This period coincides with the size of one pattern unit $r_{pattern}$, as indicated in Figure 5b. Not only does this pattern unit contain the object of interest (i.e. the square pillar), but it also encompasses the surrounding voids between it and the adjacent pillar. Specifically, the gliding box of size $r_{pattern}$ = 110 pixels in Figure 5b contains one square pillar (foreground pixels) and an L-shaped gap (background pixels). Even if the box is displaced to another location within the image, as shown in Figure 5b, it will still cover roughly the same number of foreground and background pixels. On the other hand, a gliding box of $1.5r_{pattern}$ may cover a total of more than two square pillars in one location to slightly more than one pillar in another location. As a result, $s_k(r = r_{pattern}) < s_k(r = 1.5r_{pattern})$. The dip in $s_k(r)$ also occurs for $2r_{pattern}$, $3r_{pattern}$,…$nr_{pattern} < M$, where n is an integer, and this explains why $s_k(r)$ oscillates in Figure 5a.

Therefore, for a set in which objects of interest are regularly spaced, the pattern size cannot be determined from detecting changes in the slope of the $\lambda(r)$ curve, as suggested by Plotnick *et al*. (Plotnick, et al., 1996), but rather by measuring the period of oscillations of $s_k(r)$ or $\lambda(r)$ about 1, which begin at $r = r_{pattern}$. In cases where $\lambda(r)$ does not exhibit oscillations, such as the laser-induced structures displayed in Figures 2 and 3, determining pattern sizes from $\lambda(r)$

plots should be avoided due to the ambiguity involved in deciding where the slope changes abruptly.

5. Conclusion

In conclusion, we have shown that the spatial heterogeneity of hierarchical surface topographies can be successfully quantified using lacunarity analysis, which allows for the objective characterization and comparison of surface topographies. On the other hand, the box-counting fractal dimension (D_{BC}) was found to be a poor descriptor for the complexity of the SEM images. We have also observed that, for surface topographies containing features having multiple length scales, lacunarity trends reverse with every order of magnitude increase in magnification as a result of the introduction of newly resolvable surface details. Finally, in cases where an image contains regularly spaced texture elements, its pattern size can be accurately determined by measuring the period of oscillations of its lacunarity curve beginning at box sizes larger than the pattern size. Lacunarity analysis is therefore a powerful tool that can be used to characterize surfaces topographies containing, but not limited to, hierarchical structures, thereby reducing the need for subjective qualitative assessments of SEM images.

6. Acknowledgements

The authors gratefully acknowledge the financial support received from the Natural Sciences and Engineering Research Council of Canada (NSERC) and the Fonds de recherche du Québec – Nature et technologies (FRQNT). We would also like to thank the McGill Plasma Processing Laboratory (PPL) for allowing the use of its scanning electron microscope for surface characterization. Finally, we thank K. M. Tanvir Ahmmed and Julien Saïd for the fabrication of laser-irradiated samples shown in Figures 2 and 3, respectively.

References

AHMMED, K., GRAMBOW, C. & KIETZIG, A.-M. (2014). Fabrication of Micro/Nano Structures on Metals by Femtosecond Laser Micromachining. Micromachines **5**(4), 1219-1253.

AHMMED, K.M.T., LING, E.J.Y., SERVIO, P. & KIETZIG, A.-M. (2015). Introducing a new optimization tool for femtosecond laser-induced surface texturing on titanium, stainless steel, aluminum and copper. Opt. Laser Eng. **66**(0), 258-268.

AL-KADI, O.S. & WATSON, D. (2008). Texture Analysis of Aggressive and Nonaggressive Lung Tumor CE CT Images. IEEE Transactions on Biomedical Engineering **55**(7), 1822-1830.

ALLAIN, C. & CLOITRE, M. (1991). Characterizing the lacunarity of random and deterministic fractal sets. Phys. Rev. A **44**(6), 3552-3558.

ALVAREZ, A.C., PASSÉ-COUTRIN, N. & GASPARD, S. (2013). Determination of the textural characteristics of carbon samples using scanning electronic microscopy images: comparison with mercury porosimetry data. Adsorption **19**(2-4), 841-850.

BARTHLOTT, W. & NEINHUIS, C. (1997). Purity of the sacred lotus, or escape from contamination in biological surfaces. Planta **202**(1), 1-8.

BHARATI, M.H., LIU, J.J. & MACGREGOR, J.F. (2004). Image texture analysis: methods and comparisons. Chemometrics and Intelligent Laboratory Systems **72**(1), 57-71.

BHUSHAN, B. (2012). *Biomimetics: Bioinspired Hierarchical-Structured Surfaces for Green Science and Technology*. Berlin: Springer-Verlag Berlin Heidelberg.

BHUSHAN, B., JUNG, Y.C. & KOCH, K. (2009). Micro-, nano- and hierarchical structures for superhydrophobicity, self-cleaning and low adhesion. Phil. Trans. R. Soc. **367**, 1631-1672.

BUTSON, C.R. & KING, D.J. (2006). Lacunarity analysis to determine optimum extents for sample‐based spatial information extraction from high‐resolution forest imagery. International Journal of Remote Sensing **27**(1), 105-120.

CHEN, S.S., KELLER, J.M. & CROWNOVER, R.M. (1993). On the calculation of fractal features from images. Pattern Analysis and Machine Intelligence, IEEE Transactions on **15**(10), 1087-1090.

CUTTING, J.E. & GARVIN, J.J. (1987). Fractal curves and complexity. Perception & Psychophysics **42**(4), 365-370.

DALE, M.R.T. (2000). Lacunarity analysis of spatial pattern: A comparison. Landscape Ecol **15**(5), 467-478.

DALE, M.R.T., DIXON, P., FORTIN, M.-J., LEGENDRE, P., MYERS, D.E. & ROSENBERG, M.S. (2002). Conceptual and mathematical relationships among methods for spatial analysis. Ecography **25**(5), 558-577.

DAVIES, E.R. (2008). Introduction to Texture Analysis. In *Handbook of Texture Analysis*, Mirmehdi, M., Xie, X. and Suri, J. (Eds.), pp. 1-31. London: Imperial College Press.

DEMIR, A.G., FURLAN, V., LECIS, N. & PREVITALI, B. (2014). Laser surface structuring of AZ31 Mg alloy for controlled wettability. Biointerphases **9**(2), 029009.

DUBUISSON, M.-P. & DUBES, R.C. (1994). Efficacy of fractal features in segmenting images of natural textures. Pattern Recognition Letters **15**(4), 419-431.

ELLINAS, K., TSEREPI, A. & GOGOLIDES, E. (2011). From Superamphiphobic to Amphiphilic Polymeric Surfaces with Ordered Hierarchical Roughness Fabricated with Colloidal Lithography and Plasma Nanotexturing. Langmuir **27**(7), 3960-3969.

FALCONER, K. (1990). *Fractal Geometry: Mathematical Foundations and Applications*. England: John Wiley & Sons Ltd.

FENG, J., TUOMINEN, M.T. & ROTHSTEIN, J.P. (2011). Hierarchical Superhydrophobic Surfaces Fabricated by Dual-Scale Electron-Beam-Lithography with Well-Ordered Secondary Nanostructures. Advanced Functional Materials **21**(19), 3715-3722.

GÅRDING, J. (1988). Properties of fractal intensity surfaces. Pattern Recognition Letters **8**(5), 319-324.

GEFEN, Y., MEIR, Y., MANDELBROT, B.B. & AHARONY, A. (1983). Geometric Implementation of Hypercubic Lattices with Noninteger Dimensionality by Use of Low Lacunarity Fractal Lattices. Phys. Rev. Lett. **50**(3), 145-148.

GERASOPOULOS, K., POMERANTSEVA, E., MCCARTHY, M., BROWN, A., WANG, C., CULVER, J. & GHODSSI, R. (2012). Hierarchical Three-Dimensional Microbattery Electrodes Combining Bottom-Up Self-Assembly and Top-Down Micromachining. ACS Nano **6**(7), 6422-6432.

HO, A.Y.Y., YEO, L.P., LAM, Y.C. & RODRÍGUEZ, I. (2011). Fabrication and Analysis of Gecko-Inspired Hierarchical Polymer Nanosetae. ACS Nano **5**(3), 1897-1906.

JAGDHEESH, R., PATHIRAJ, B., KARATAY, E., RÖMER, G.R.B.E. & HUIS IN'T VELD, A.J. (2011). Laser-Induced Nanoscale Superhydrophobic Structures on Metal Surfaces. Langmuir **27**(13), 8464-8469.

JELINEK, H.F. & FERNANDEZ, E. (1998). Neurons and fractals: how reliable and useful are calculations of fractal dimensions? Journal of Neuroscience Methods **81**(1–2), 9-18.

JUNG, Y.C. & BHUSHAN, B. (2010). Biomimetic structures for fluid drag reduction in laminar and turbulent flows. J Phys Condens Matter **22**(3), 035104.

KARPERIEN, A. (1999-2014). FracLac for ImageJ.

KARPERIEN, A., AHAMMER, H. & JELINEK, H. (2013). Quantitating the Subtleties of Microglial Morphology with Fractal Analysis. Frontiers in Cellular Neuroscience **7**.

KELLER, J.M., CHEN, S. & CROWNOVER, R.M. (1989). Texture description and segmentation through fractal geometry. Computer Vision, Graphics, and Image Processing **45**(2), 150-166.

KENKEL, N.C. & WALKER, D.J. (1993). Fractals and ecology. Abstracta Botanica **17**(1-2), 53-70.

KHORASANI, H., ZHENG, Z., NGUYEN, C., ZARA, J., ZHANG, X., WANG, J., TING, K. & SOO, C. (2011). A Quantitative Approach to Scar Analysis. The American Journal of Pathology **178**(2), 621-628.

KIETZIG, A.-M., HATZIKIRIAKOS, S.G. & ENGLEZOS, P. (2009). Patterned Superhydrophobic Metallic Surfaces. Langmuir **25**(8), 4821-4827.

LEHR, J. & KIETZIG, A.-M. (2014). Production of homogenous micro-structures by femtosecond laser micro-machining. Opt. Laser Eng. **57**(0), 121-129.

LING, E.J.Y., SAÏD, J., BRODUSCH, N., GAUVIN, R., SERVIO, P. & KIETZIG, A.-M. (2015). Investigating and understanding the effects of multiple femtosecond laser scans on the surface topography of stainless steel 304 and titanium. Appl. Surf. Sci. **353**(0), 512-521.

MALHI, Y. & ROMÁN-CUESTA, R.M. (2008). Analysis of lacunarity and scales of spatial homogeneity in IKONOS images of Amazonian tropical forest canopies. Remote Sensing of Environment **112**(5), 2074-2087.

MANDELBROT, B.B. (1983). *The fractal geometry of nature*. New York, USA: W. H. Freeman and Company.

MANERA, M., DEZFULI, B.S., BORRECA, C. & GIARI, L. (2014). The use of fractal dimension and lacunarity in the characterization of mast cell degranulation in rainbow trout (Onchorhynchus mykiss). Journal of Microscopy **256**(2), 82-89.

MORADI, S., KAMAL, S., ENGLEZOS, P. & HATZIKIRIAKOS, S.G. (2013). Femtosecond laser irradiation of metallic surfaces: effects of laser parameters on superhydrophobicity. Nanotechnology **24**(41), 415302.

MYINT, S.W. & LAM, N. (2005). A study of lacunarity-based texture analysis approaches to improve urban image classification. Computers, Environment and Urban Systems **29**(5), 501-523.

NAKAYAMA, K., TSUJI, E., AOKI, Y. & HABAZAKI, H. (2014). Fabrication of superoleophobic hierarchical surfaces for low-surface-tension liquids. RSC Advances **4**(58), 30927-30933.

NAYAK, B.K. & GUPTA, M.C. (2010). Self-organized micro/nano structures in metal surfaces by ultrafast laser irradiation. Opt. Laser Eng. **48**(10), 940-949.

NEUMANN, G.T. & HICKS, J.C. (2012). Novel Hierarchical Cerium-Incorporated MFI Zeolite Catalysts for the Catalytic Fast Pyrolysis of Lignocellulosic Biomass. ACS Catalysis **2**(4), 642-646.

NOH, J., LEE, J.-H., NA, S., LIM, H. & JUNG, D.-H. (2010). Fabrication of Hierarchically Micro- and Nano-structured Mold Surfaces Using Laser Ablation for Mass Production of superhydrophobic Surfaces. Jpn. J. Appl. Phys. **49**, 106502.

NOSONOVSKY, M. & BHUSHAN, B. (2008). *Multiscale Dissipative Mechanisms and Hierarchical Surfaces : Friction, Superhydrophobicity, and Biomimetics*. Berlin Heidelberg: Springer-Verlag.

PALAZOGLU, A., STROEVE, P. & ROMAGNOLI, J.A. (2010). Wavelet analysis of images from scanning probe and electron microscopy. In *Microscopy: Science, Technology, Applications and Education*, Méndez-Vilas, A. and Díaz, J. (Eds.), pp. 1251-1262. Badajoz, Spain: Formatex.

PENTLAND, A.P. (1984). Fractal-Based Description of Natural Scenes. Pattern Analysis and Machine Intelligence, IEEE Transactions on **PAMI-6**(6), 661-674.

PLOTNICK, R.E., GARDNER, R.H., HARGROVE, W.W., PRESTEGAARD, K. & PERLMUTTER, M. (1996). Lacunarity analysis: A general technique for the analysis of spatial patterns. Physical Review E **53**(5), 5461-5468.

PLOTNICK, R.E., GARDNER, R.H. & O'NEILL, R.V. (1993). Lacunarity indices as measures of landscape texture. Landscape Ecol **8**(3), 201-211.

RASBAND, W. (1997-2014). ImageJ.

RIVERA-VIRTUDAZO, R., TAPIA, A., VALENZUELA, J., CRUZ, L., MENDOZA, H. & CASTRICIONES, E. (2009). Lacunarity Analysis of TEM Images of Heat-Treated Hybrid Organosilica Materials. In *Innovations in Chemical Biology*, Şener, B. (Ed.), pp. 397-403. Springer Netherlands.

SARKAR, N. & CHAUDHURI, B.B. (1994). An efficient differential box-counting approach to compute fractal dimension of image. Systems, Man and Cybernetics, IEEE Transactions on **24**(1), 115-120.

SAUNDERS, S.C., CHEN, J., DRUMMER, T.D., GUSTAFSON, E.J. & BROSOFSKE, K.D. (2005). Identifying scales of pattern in ecological data: a comparison of lacunarity, spectral and wavelet analyses. Ecological Complexity **2**(1), 87-105.

SHAO, F., SUN, J., GAO, L., YANG, S. & LUO, J. (2011). Template-Free Synthesis of Hierarchical TiO2 Structures and Their Application in Dye-Sensitized Solar Cells. ACS Applied Materials & Interfaces **3**(6), 2148-2153.

SMITH JR, T.G., LANGE, G.D. & MARKS, W.B. (1996). Fractal methods and results in cellular morphology — dimensions, lacunarity and multifractals. Journal of Neuroscience Methods **69**(2), 123-136.

TUCERYAN, M. & JAIN, A.K. (1998). Texture Analysis. In *The Handbook of Pattern Recognition and Computer Vision* Chen, C. H. and Pau, L. F. (Eds.), pp. 207-248.

UPDIKE, S.X. & NOWZARI, H. (2008). Fractal analysis of dental radiographs to detect periodontitis-induced trabecular changes. Journal of Periodontal Research **43**(6), 658-664.

UPPAL, S.O., VORONINE, D.V., WENDT, E. & HECKMAN, C.A. (2010). Morphological Fractal Analysis of Shape in Cancer Cells Treated with Combinations of Microtubule-Polymerizing and -Depolymerizing Agents. Microscopy and Microanalysis **16**(04), 472-477.

UTRILLA-COELLO, R.G., BELLO-PÉREZ, L.A., VERNON-CARTER, E.J., RODRIGUEZ, E. & ALVAREZ-RAMIREZ, J. (2013). Microstructure of retrograded starch: Quantification from lacunarity analysis of SEM micrographs. Journal of Food Engineering **116**(4), 775-781.

WANG, H., ZHOU, H., GESTOS, A., FANG, J. & LIN, T. (2013). Robust, Superamphiphobic Fabric with Multiple Self-Healing Ability against Both Physical and Chemical Damages. ACS Applied Materials & Interfaces **5**(20), 10221-10226.

WORKMAN, M.J., SEROV, A., HALEVI, B., ATANASSOV, P. & ARTYUSHKOVA, K. (2015). Application of the Discrete Wavelet Transform to SEM and AFM Micrographs for Quantitative Analysis of Complex Surfaces. Langmuir **31**(17), 4924-4933.

YAŞAR, F. & AKGÜNLÜ, F. (2005). Fractal dimension and lacunarity analysis of dental radiographs. Dentomaxillofacial Radiology **34**(5), 261-267.

ZHANG, J., HUANG, W. & HAN, Y. (2006). Wettability of Zinc Oxide Surfaces with Controllable Structures. Langmuir **22**(7), 2946-2950.

ZHANG, M., SHAO, C., GUO, Z., ZHANG, Z., MU, J., ZHANG, P., CAO, T. & LIU, Y. (2011). Highly Efficient Decomposition of Organic Dye by Aqueous-Solid Phase Transfer and In Situ Photocatalysis Using Hierarchical Copper Phthalocyanine Hollow Spheres. ACS Applied Materials & Interfaces **3**(7), 2573-2578.

ZHU, T., LI, J. & WU, Q. (2011). Construction of TiO2 Hierarchical Nanostructures from Nanocrystals and Their Photocatalytic Properties. ACS Applied Materials & Interfaces **3**(9), 3448-3453.

ZOU, M., BECKFORD, S., WEI, R., ELLIS, C., HATTON, G. & MILLER, M.A. (2011). Effects of surface roughness and energy on ice adhesion strength. Appl. Surf. Sci. **257**, 3786-3792.

Figure Captions

Figure 1. a) Koch snowflake. b) Schematic demonstrating the gliding box-counting algorithm for the lacunarity analysis of a binary image of size M. Foreground (white) and background (black) pixels are designated by '1' and '0' boxes, respectively.

Figure 2. Log-log plot of $\lambda(r)$ against r of the SEM images shown in a) undulating grooves on stainless steel 304, b) columnar structures on stainless steel 304, c) maze-like structures on aluminum, d) layered bumps on aluminum, and e) chaotic structures on stainless steel 304. The images shown in a) to e) are representative subsets cropped from the original 1024 x 1023 images so that the surface topographies can be better perceived. However, $\lambda(r)$ was evaluated for the entire original image (1024 x 1023 pixels).

Figure 3. Log-log plot of $\lambda(r)$ against r tracking the evolution of laser-induced columnar structures formed on stainless steel 304 as a function of the number of fs-laser scans (N_s). The steel sample was irradiated at a peak fluence of 1.1 J/cm^2 and with 756 pulses-per-spot. The SEM images shown in a) to e) are representative subsets cropped from the original 1024 x 882 images so that the surface topographies can be better perceived. However, $\lambda(r)$ was evaluated for the entire original image (1024 x 882 pixels).

Figure 4. Lacunarity plots of SEM images, obtained at different magnifications, of laser-inscribed square pillars machined on copper. a) 150x-1500x magnification. Square markers correspond to the measured pixel width of the square pillars. b) 1500x-15,000x magnification. c)

15,000x-120,000x magnification. The SEM images d) to g) represent the entire image (1024 x 882).

Figure 5. a) The mean pixel count $\bar{k}(r)$ and the standard deviation $s_k(r)$ as a function of the box size r. b) Binary SEM image of laser-inscribed square pillars obtained at 300x magnification.

Figure S1. Lacunarity plots of SEM images, obtained at different magnifications, of laser-inscribed square pillars machined on copper. a) 150x-1500x magnification. Square markers correspond to the measured pixel width of the square pillars. b) 1500x-15,000x magnification. c) 15,000x-120,000x magnification. The SEM images d) to g) represent the entire image (1024 x 882). The laser-inscribed surface topography analyzed here was fabricated under different processing conditions than those shown in Figure 4 of the main manuscript.

FIGURE 1

FIGURE 2

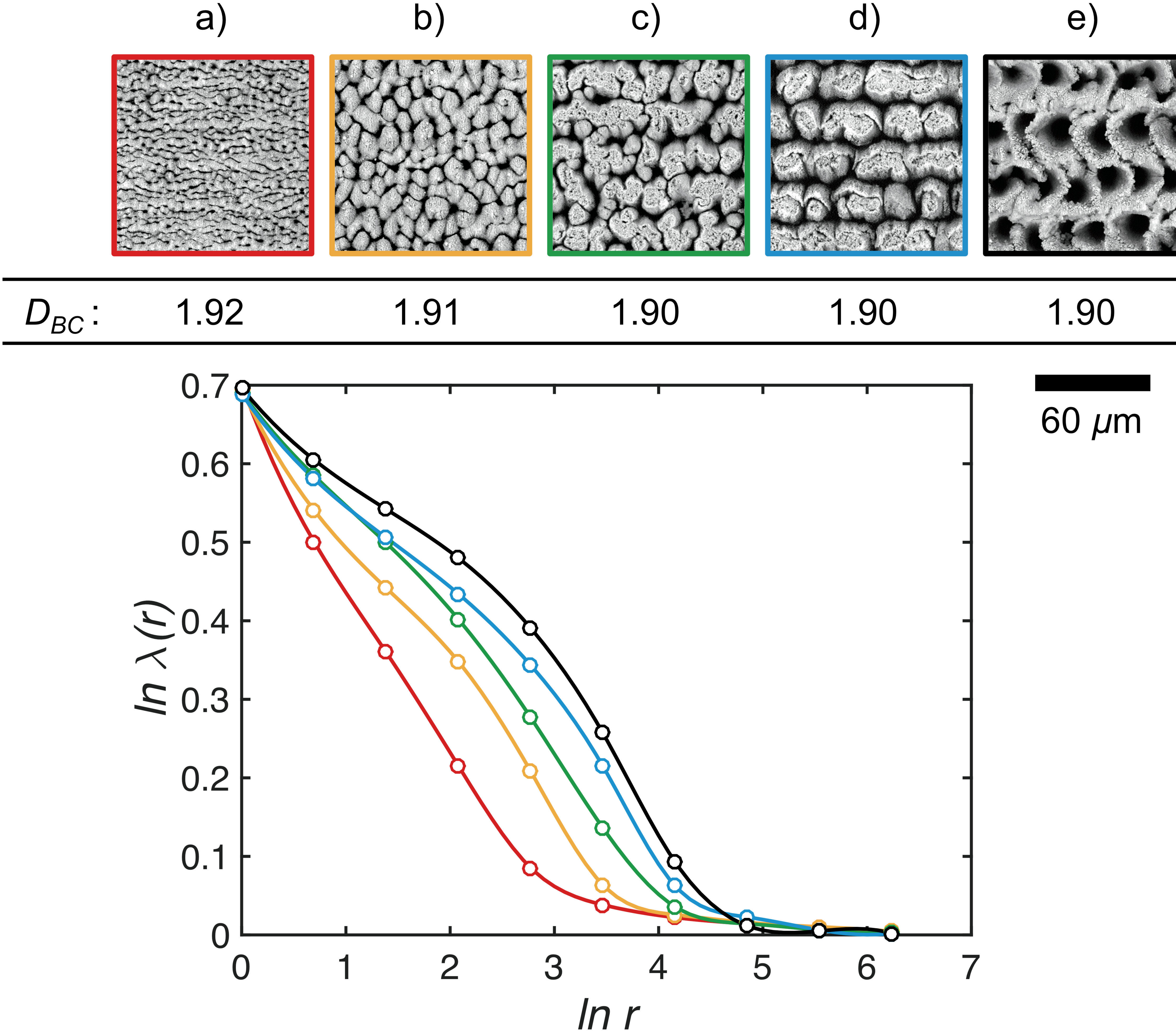

a)
b)
c)
d)
e)
D_{BC}:
1.92
1.91
1.90
1.90
1.90
60 μm
0.7
0.6
0.5
0.4
0.3
0.2
0.1
0
$ln\ \lambda(r)$
0
1
2
3
4
5
6
7
$ln\ r$

FIGURE 3

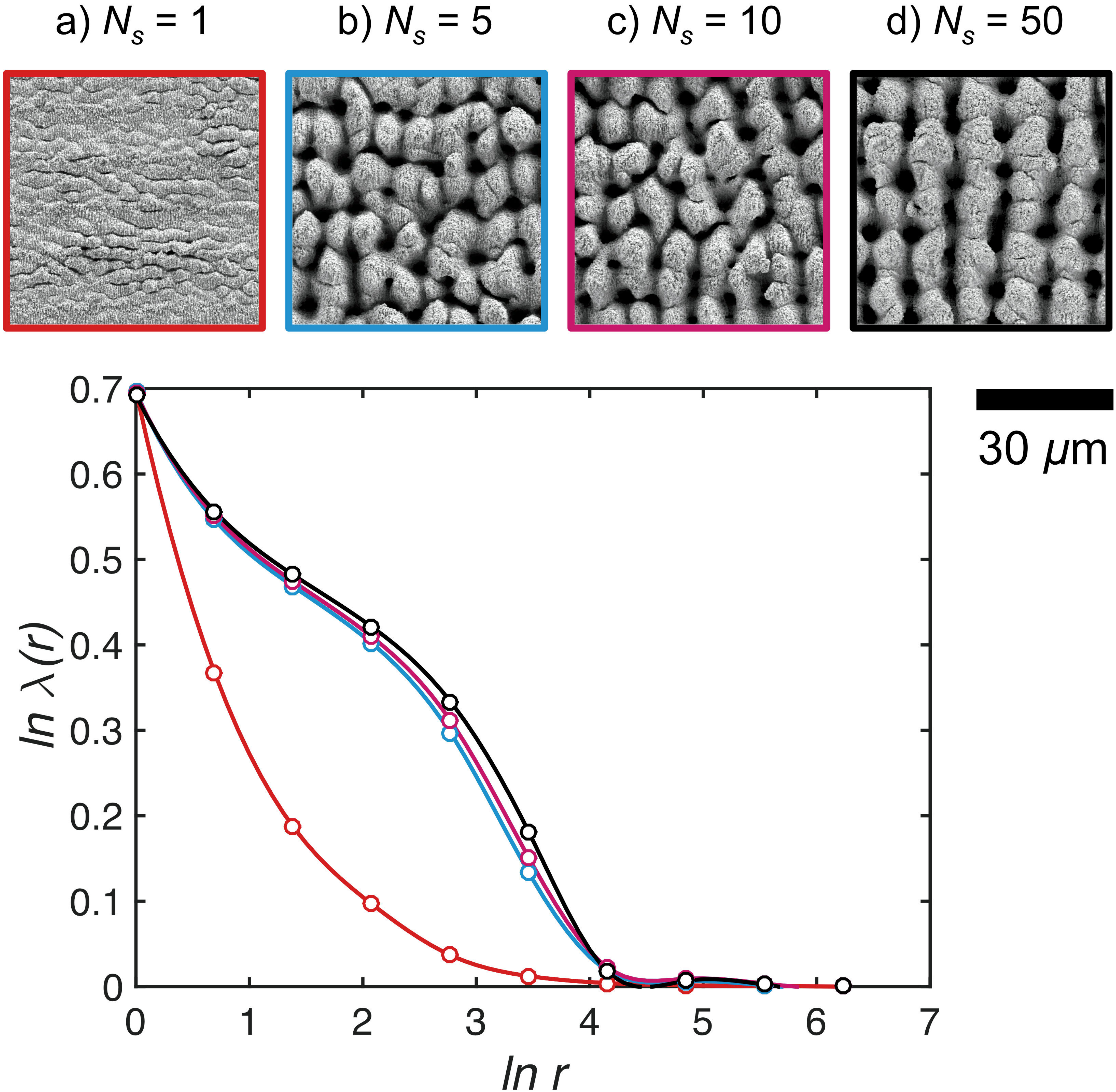
a) N_s = 1
b) N_s = 5
c) N_s = 10
d) N_s = 50
30 μm
0.7
0.6
0.5
0.4
0.3
0.2
0.1
0
ln λ(r)
0
1
2
3
4
5
6
7
ln r

FIGURE 4

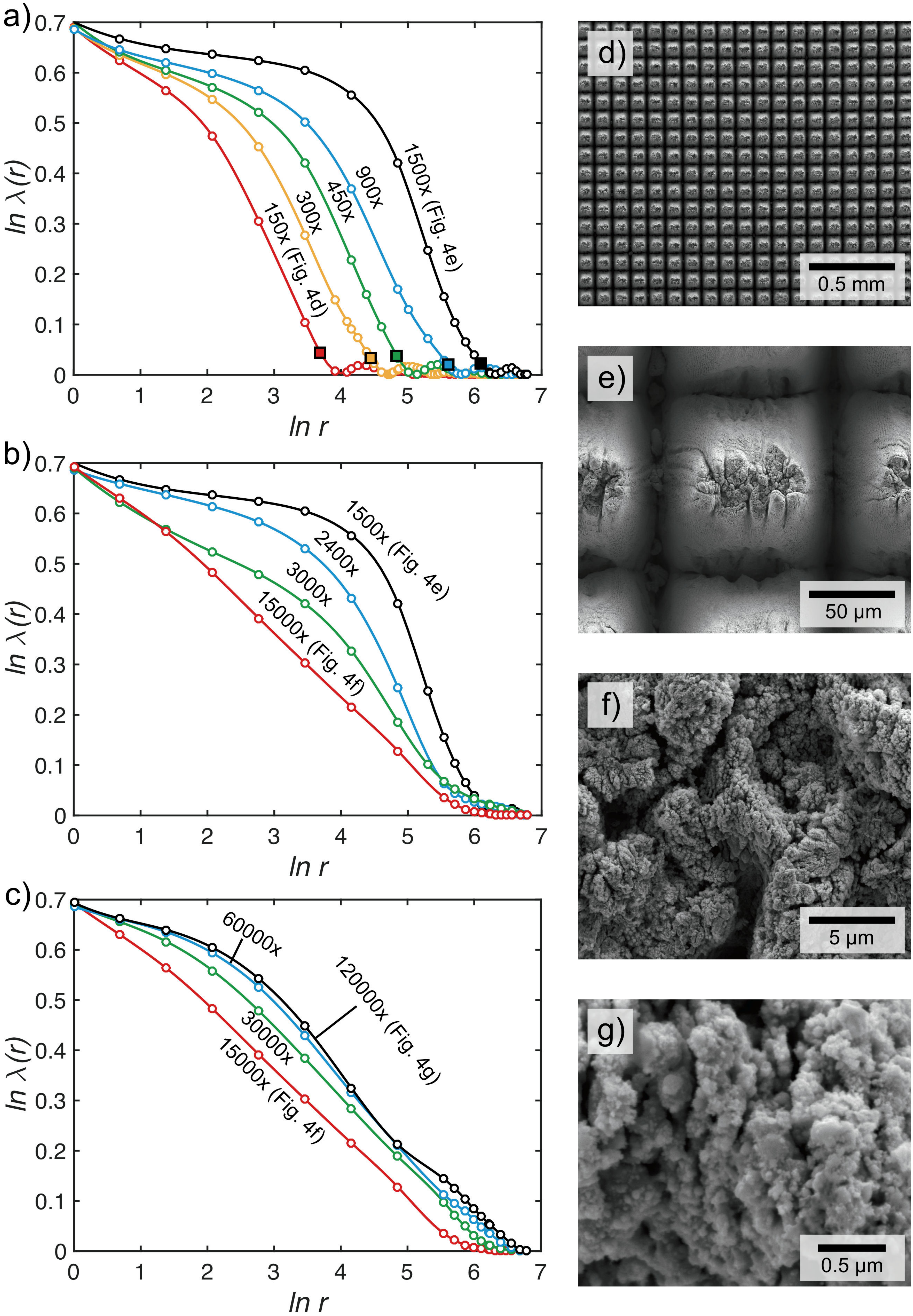

a)
b)
c)
ln λ(r)
ln r
150x (Fig. 4d)
300x
450x
900x
1500x (Fig. 4e)
2400x
3000x
15000x (Fig. 4f)
30000x
60000x
120000x (Fig. 4g)
d)
0.5 mm
e)
50 µm
f)
5 µm
g)
0.5 µm

FIGURE 5

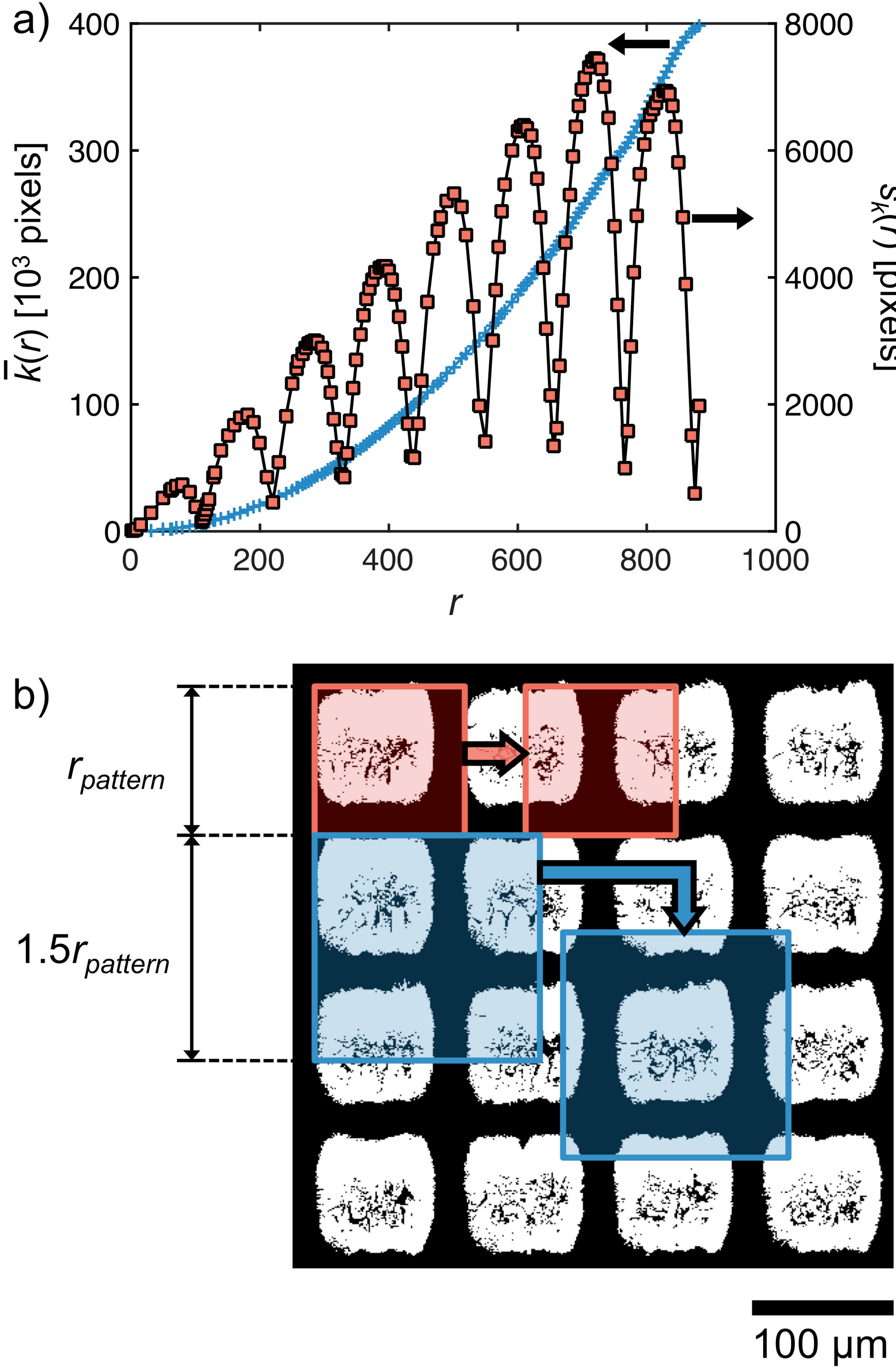

a)
$\bar{k}(r)$ [10^3 pixels]
$s_k(r)$ [pixels]
r
0
100
200
300
400
0
2000
4000
6000
8000
0
200
400
600
800
1000
b)
$r_{pattern}$
$1.5r_{pattern}$
100 µm

FIGURE S1

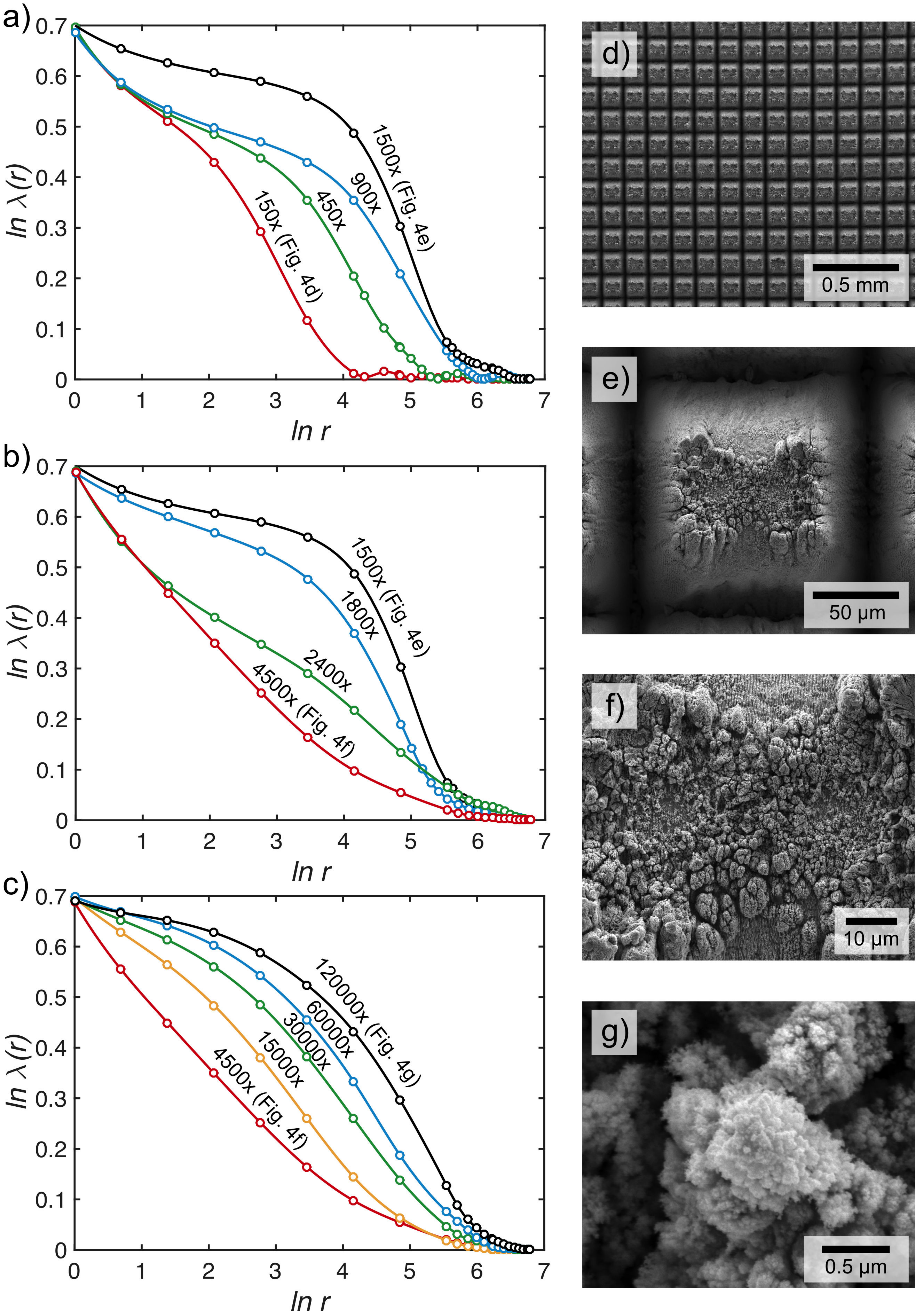
a)
b)
c)
d)
e)
f)
g)
ln λ(r)
ln r
1500x (Fig. 4e)
900x
450x
150x (Fig. 4d)
1800x
2400x
4500x (Fig. 4f)
120000x (Fig. 4g)
60000x
30000x
15000x
0.5 mm
50 μm
10 μm
0.5 μm